Metallomics, 14, 2022, mfac072
https://doi.org/10.1093/mtomcs/mfac072
Advance access publication date: 23 September 2022
Paper

Ursolic acid-piperazine-dithiocarbamate ruthenium(II) polypyridyl complexes induced necroptosis in MGC-803 cells

Hong Jiang [1,‡], Jian-Hua Wei [1,2,3,*,‡], Cui-Yan Lin [1,‡], Gui-Bin Liang[1], Rui-Jie He [4], Ri-Zhen Huang [1,*], Xian-Li Ma [1], Guo-Bao Huang [2] and Ye Zhang [1,2,3,*]

[1]Guangxi Engineering Research Center for Pharmaceutical Molecular Screening and Druggability Evaluation, School of Pharmacy, Guilin Medical University, Guilin 541199, China, [2]Guangxi Key Laboratory of Agricultural Resources Chemistry and Biotechnology, College of Chemistry and Food Science, Yulin Normal University, Yulin 537000, China, [3]State Key Laboratory for Chemistry and Molecular Engineering of Medicinal Resources, School of Chemistry and Pharmacy, Guangxi Normal University, Guilin 541004, China and [4]Guangxi Key Laboratory of Plant Functional Phytochemicals and Sustainable Utilization, Guangxi Institute of Botany, Guangxi Zhuang Autonomous Region and Chinese Academy of Sciences, Guilin 541006, China
*__Correspondence:__ 1 Zhiyuan Road, Lingui District, School of Pharmacy, Guilin Medical University, Guilin 541199, Guangxi, P.R. China. E-mail: weijh1124@glmc.edu.cn (Jian-Hua Wei); rzhuang1783@163.com (Ri-Zhen Huang); zhangye81@126.com (Ye Zhang)
‡These authors contributed equally to this work.
Electronic Supplementary Information (ESI) available. See DOI: 10.1039/x0xx000 00x.

Abstract

Three ursolic acid-piperazine-dithiocarbamate ruthenium(II) polypyridyl complexes **Ru1–Ru3** were designed and synthesized for evaluating antitumor activity. All the complexes exhibited high *in vitro* cytotoxicity against MGC-803, T24, HepG2, CNE2, MDA-MB-231, MCF-7, A549, and A549/DDP cell lines. **Ru1**, **Ru2**, and **Ru3** were 11, 8 and 10 times, respectively, more active than cisplatin against A549/DDP. An *in vivo* study on MGC-803 xenograft mouse models demonstrated that representative **Ru2** exhibited an effective inhibitory effect on tumor growth, showing stronger antitumor activity than cisplatin. Biological investigations suggested that **Ru2** entered MGC-803 cells by a clathrin-mediated endocytic pathway, initially localizing in the lysosomes and subsequently escaping and localizing in the mitochondria. Mitochondrial swelling resulted in vacuolization, which induced vacuolation-associated cell death and necroptosis with the formation of necrosomes (RIP1–RIP3) and the uptake of propidium iodide. These results demonstrate that the potential of **Ru2** as a chemotherapeutic agent to kill cancer cells via a dual mechanism represents an alternative way to eradicate apoptosis-resistant forms of cancer.

Keywords: ursolic acid-piperazine-dithiocarbamate, ruthenium (II) polypyridyl complexes, antitumor activity, action mechanism, vacuolation-associated cell death

Graphical abstract

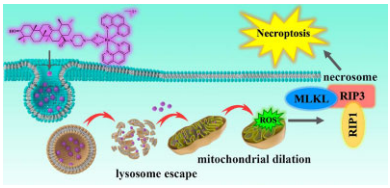

One ursolic acid-piperazine-dithiocarbamate ruthenium (II) polypyridyl complex (**Ru2**) as a potential chemotherapeutic agent was developed. **Ru2** exhibited significant anticancer activities in *vitro* and *vivo*. Biological investigation suggested that it entered MGC-803 cells by a clathrin-mediated endocytic pathway, initially localizing in the lysosomes and subsequently escaping and localizing in the mitochondria. Mitochondrial swelling results in vacuolization, which induced vacuolation-associated cell death and necroptosis.

Introduction

Drug resistance, which involves increments in drug efflux and decreased DNA repair ability,[1] and alterations in apoptotic pathways, is still recognized as a great challenge in chemotherapy.[2–4] Since many therapeutic agents exert their antitumor effects by inducing intrinsic apoptosis,[5] alternative nonapoptotic cell death pathways have been explored and proven to be a feasible strategy for killing apoptotic-resistant tumor cells. As a form of programmed cell death featured by necrotic cell death morphology and autophagy activation, necroptosis represents a novel non-apoptotic cell death pathway and has been proven to play a significant role in multiple pathologies, including carcinoma, inflammation, and sepsis.[6] Necroptosis is now forged as a promising

Received: May 1, 2022. **Accepted:** August 31, 2022

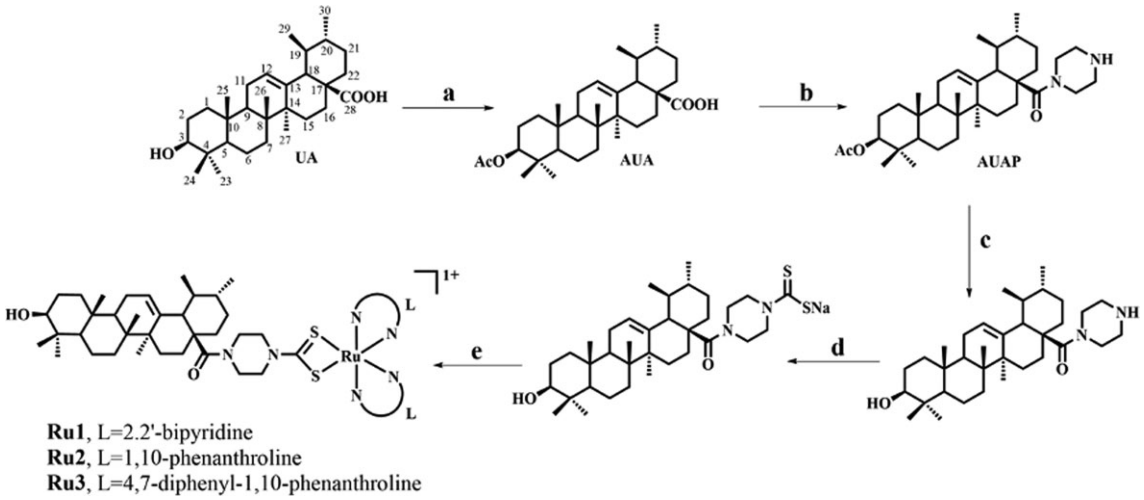

Scheme 1 Synthetic routes of **Ru1–Ru3**. Reagents and conditions: (a) Ac_2O/DMAP/pyridine, r.t; (b) i: ClCOCOCl/CH_2Cl_2, r.t; ii: Et_3N/CH_2Cl_2, piperazine; (c) 4 mol/l NaOH aq, THF/MeOH, r.t; (d) CS_2, NaOH, r.t; (e) Dichlorobis(2,2-bipyridine) ruthenium(II) (**A**)/Dichlorobis(1,10-phenanthroline) ruthenium(II) (**B**)/Dichlorobis(4,7-diphenyl-1,10-phenanthroline) ruthenium(II) (**C**), 65°C.

therapeutic form for cancer therapy.[7] Therefore, the identification of necroptosis inducers/inhibitors has drawn special attention and may create an evolution of new chemotherapy interventions. Necroptosis has been proven to implicate the formation of receptor-interacting protein (RIP) kinases: RIP1–RIP3 complex, which could mediate oxidative stress and lead to the generation of mitochondrial reactive oxygen species (ROS), and consequently, cause the induction of bioenergetic-related cell death.[8–10]

Since the discovery of platinum antitumor complexes, including cisplatin, carboplatin, and oxaliplatin, a great deal of effort has been devoted to developing metal antitumor complexes with various physicochemical, biological, and pharmacological diversities. Among the numerous metal antitumor complexes, ruthenium complexes have attracted considerable attention because of their good coordinative ability, relatively low toxicity, and potential antitumor virtue.[11] As an important form of ruthenium antitumor complexes, ruthenium(II) polypyridyl complexes have exhibited attractive antitumor properties and exerted antitumor effects by multiple action mechanisms, including DNA damage, topoisomerase (topo I or/and II) inhibition, apoptosis induction, and cell cycle arrest.[12–14] Small structural modifications to ruthenium(II) polypyridyl complexes could have a significant influence on their antitumor effect and mechanism.

Traditional Chinese medicine (TCM) is an indispensable part of Chinese culture and has been proven to play an important role in antitumor therapy.[15] As a well-known TCM ingredient, ursolic acid (**UA**) and its derivatives have been demonstrated to display attractive antitumor activity.[16–19] A recent study has indicated that UA could exert antitumor activity through a necroptosis mechanism.[20] The potential antitumor effect of **UA** and its derivatives encouraged us to design, synthesize and evaluate **UA** derivatives as antitumor agents. In addition, piperazine is considered as a lysosome-targeting privileged scaffold in antitumor drug discovery and has widely involved in many therapeutic agents, while lysosomes are important organelles in animal cells and play a crucial role in many cellular processes.[21] The special virtue of piperazine prompted us to introduce it to **UA** skeleton to screen for antitumor agents. Moreover, since the antitumor effect and mechanism of the old alcohol-aversion drug disulfiram has been elucidated,[22] a great deal of attention has been devoted to the design, synthesis and evaluation dithiocarbamato antitumor derivatives with high efficiency and low toxicity. Dithiocarbamato is considered as a special coordination group for antitumor complexes, and some dithiocarbamato ruthenium complexes have exhibited potent antiproliferative activity.[23] In our previous work, we have synthesized and evaluated some dehydroabietyl piperazine dithiocarbamate ruthenium(II) polypyridyl complexes as potential antitumor agents,[24] by the combination of dehydroabietic acid (a TCM active ingredient), piperazine, dithiocarbamato and ruthenium(II) polypyridyl.

Recently, some ruthenium polypyridyl complexes have been evaluated as anticancer agents, including as photosensitizers in photodynamic therapy, most of which induce tumor cell death through apoptosis.[25–27] However, as mentioned above, drug resistance involves the alteration in apoptotic pathways. It is extremely difficult to treat cancer with apoptotic resistance. And it is of great interest to design ruthenium polypyridyl complexes with high anticancer activity and non-apoptotic mechanisms. Based on the above research background, we designed and introduced the piperazine and dithiocarbamato groups into the **UA**-active core to offer a ligand, which was then coordinated with ruthenium polypyridyl intermediated to offer $[Ru(bpy)_2(L)]Cl$ **Ru1**, $[Ru(phen)_2(L)]Cl$ **Ru2**, and $[Ru(DIP)_2(L)]Cl$ **Ru3**, respectively. To the best of our knowledge, the design, synthesis, antitumor activity and mechanisms evaluation of **UA**-piperazine-dithiocarbamate ruthenium polypyridyl complexes have not been described in the literature. Our experimental results revealed that **Ru2** exhibited significant anticancer activities in *vitro* and *vivo*, as well as effectively inhibited the proliferation of cisplatin-resistant cells A549/DDP. Notably, **Ru2** induced MGC-803 cancer cell death mainly through necroptosis.

Results and discussion

Chemistry

The ligand **UA**-piperazine-dithiocarbamate (**L**) and its three complexes **Ru1–Ru3** were synthesized as outlined in Scheme 1. Firstly, acetyl **UA** (**AUA**) was synthesized by the acetylation of **UA** with the acetic anhydride/pyridine/4-dimethylaminopyridine (DMAP) acetyl system, according to our previous work.[19] Secondly, **AUA** was treated with oxalyl chloride to offer acetyl **UA** chloride, which was then reacted with piperazine in

Table 1 IC_{50} (μM) values of the compounds toward different cell lines after 48-h incubation

Compd.	IC_{50}(μM)					
	MGC-803	T24	HepG2	CNE2	MDA-MB-231	MCF-7
Ru1	0.96 ± 0.01	1.77 ± 0.03	2.88 ± 0.12	1.34 ± 0.21	2.41 ± 0.37	1.16 ± 0.34
Ru2	0.73 ± 0.12	0.99 ± 0.62	2.09 ± 0.89	2.43 ± 0.36	1.95 ± 0.11	3.25 ± 0.50
Ru3	10.35 ± 0.11	2.65 ± 0.37	41.22 ± 0.29	>50	5.46 ± 0.32	14.63 ± 0.12
L	19.61 ± 0.36	11.16 ± 0.89	8.68 ± 0.10	>50	12.10 ± 0.61	10.46 ± 0.27
A	15.51 ± 0.16	9.16 ± 0.16	29.03 ± 0.63	15.34 ± 0.49	8.39 ± 0.02	8.94 ± 0.46
B	>50	>50	>50	>50	>50	>50
C	>50	>50	>50	>50	>50	>50
cisplatin	9.99 ± 0.13	14.74 ± 0.18	12.94 ± 0.75	4.14 ± 0.23	>50	21.51 ± 0.58

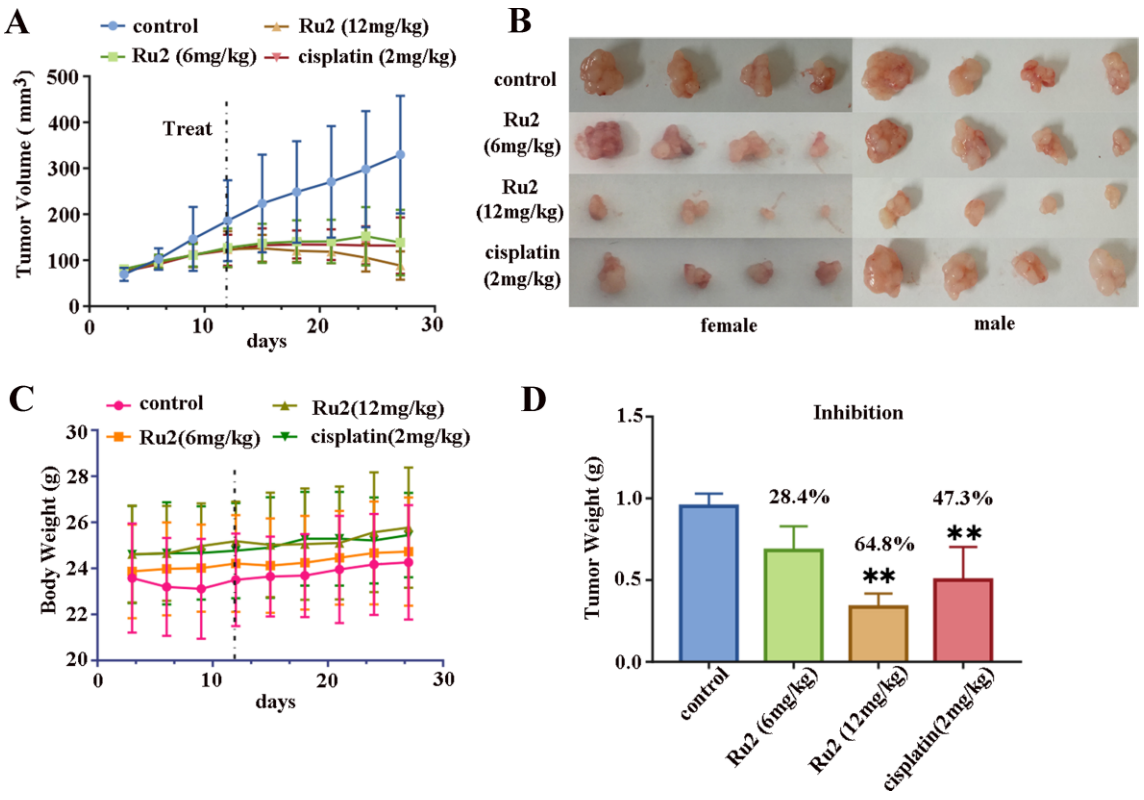

Fig. 1 In vivo antitumor activity of **Ru2** in MGC-803 xenograft. (A) **Ru2** (at 6 and 12 mg/kg doses), cisplatin (at 2 mg/kg dose), or vehicle (5% DMSO in saline, v/v) was administered by tail vein injection to inhibit tumor growth. Tumor growth was monitored by the mean tumor volume (mm3) ±SD (n = 4) and calculated as the relative tumor increment rate (T/C, %). (B) Photographs of the harvested tumors from the mice. (C) Body weight change in the mice treated with **Ru2**. (D) Tumor weight of the mice. The tumors were collected from the mice on day 27 (**$P < 0.01$).

dichloromethane to provide the **AUA** piperazine (**AUAP**) in the presence of trimethylamine. Thirdly, **AUAP** was hydrolyzed with 4 mol/l NaOH aqueous solution to offer the important intermediate compound **UA** piperazine (**UAP**) in the presence of the mixture of tetrahydrofuran and methanol. **UAP** was then treated with carbon disulfide in dichloromethane to supply the target ligand **UAP**-dithiocarbamate (**L**) in good yield in the presence of sodium hydroxide. Finally, three UA-piperazine-dithiocarbamate ruthenium(II) polypyridyl target complexes **Ru1–Ru3** were obtained in moderate yield by the treatment of **L** with di(2,2'-bipyridine, bpy) ruthenium(II) dichloride (**A**), di(1,10-phenanthroline, phen) ruthenium(II) dichloride (**B**), and di(4, 7-diphenyl-1,10-phenanthroline, DIP) ruthenium dichloride (**C**) at 65°C in methanol, respectively.

The structures of ligand **L** and its three complexes **Ru1–Ru3** were then identified by 1D and 2D NMR (^{1}H NMR, ^{13}C NMR, ^{1}H-^{1}H COSY NMR), high-resolution mass spectrometry (HR-MS), and/or elemental analysis (EA). For the ligand **L**, in ^{1}H NMR, the chemical shift (δ) in 5.09 ppm was attributed to the hydrogen in the olefin (12-H) moiety. The broad peaks at δ in the range of 4.35–3.51 ppm were ascribed to four methylene hydrogens in the piperazine group, while δ at 0.6–1.04 ppm was attributed to seven methyl hydrogens (23-CH_3, 24-CH_3, 25-CH_3, 26-CH_3, 27-CH_3, 29-CH_3, and 30-CH_3) in the UA skeleton. In the ^{13}C NMR spectra, δ at 194.45 and 174.97 ppm was attributed to the carbons in the thiocarbonyl (C=S) and carbonyl (28-C=O) groups, respectively, while δ at 124.85 (12-C) and 139.00 ppm (13-C) was attributed to the double bond carbon in the olefin moiety. In HR-MS, the mass peaks at

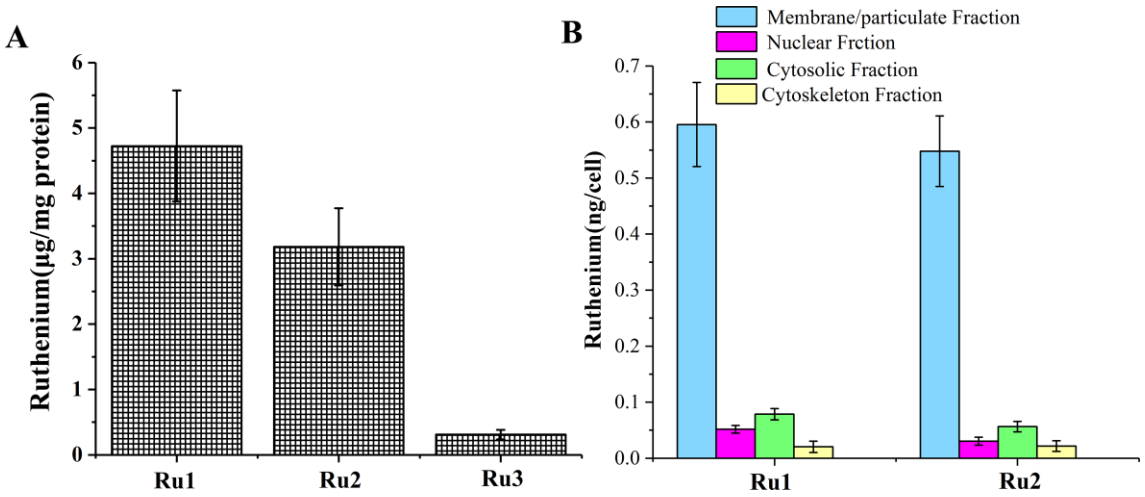

Fig. 2 (A) Intracellular ruthenium concentrations in whole cells for **Ru1-Ru3**(μg/mg protein,). (B) Cellular fractionsn for **Ru1** and **Ru2** (ng/cell).

645.3597 and 599.3714 m/z were ascribed to [**L** + Na]$^+$ and [**L**-Na]$^-$, respectively, accurately confirming the structure of the ligand **L**.

For complexes **Ru1–Ru3**, in ^{1}H NMR, the chemical shift (δ) in the range of 7.31–10.02 ppm was contributed by the aromatic hydrogens in the polypyridyl ruthenium moiety, while all the hydrogen peaks were similar to that of ligand **L**, indicating that ligand **L** had a coordination reaction with polypyridyl ruthenium. In ^{13}C NMR spectra, δ around 212 and 173 ppm were ascribed to the carbons in the thiocarbonyl and carbonyl groups, respectively, while δ in the range of 123−158 ppm was attributed to the aromatic carbon in the polypyridyl moiety group and the double bond carbon in the olefin moiety, confirming the coordination effect of ligand **L** with polypyridyl ruthenium.

In HR-MS, the clean mass peaks at 1013.4136, 1061.4137, and 1365.5375 m/z were ascribed to $[C_{55}H_{71}N_6O_2RuS_2]^+$ (complex **Ru1**), $[C_{59}H_{71}N_6O_2RuS_2]^+$ (complex **Ru2**), and $[C_{83}H_{87}N_6O_2RuS_2]^+$ (complex **Ru3**), accurately verifying the structure of complexes **Ru1–Ru3**.

To investigate the purity of **Ru1–Ru3**, ultraperformance liquid chromatography (UPLC) assays were carried out with the isopropanol/methanol/water mobile phase. As shown in Figs. S2-1 to S2-3, the purity of complexes **Ru1–Ru3** was higher than 95%. In addition, **Ru1–Ru3** were stable in the mixed solution of methanol and cell culture medium after 24-h incubation (Figs. S3-1 to S3-3).

In EA, the data of C, H, and N atoms were consistent with that in NMR and HR-MS, well proving the structures of **Ru1–Ru3**. Based on the 1D and 2D NMR, HR-MS, EA, and UPLC results, the chemical structures of the complexes **Ru1–Ru3** were well characterized and identified.

Antiproliferative activity

In vitro antiproliferative activity

To investigate the *in vitro* antiproliferative activity of ruthenium polypyridyl chloride intermediate **A**–**C**, the ligand, and its complexes **Ru1**–**Ru3**, the 3-(4,5-dimethyl-2-thiazolyl)-2,5-diphenyl-2-H-tetrazolium bromide (MTT) assay was carried out against several cancer cell lines, including human gastric cancer cells MGC-803, human bladder cancer cells T24, human liver cancer cells HepG2, human nasopharyngeal cancer cells CNE2, human breast cancer cells MDA-MB-231 and MCF-7, human hepatoma cellA549. Cisplatin was used as the positive control.

As shown in Table 1, the complexes **Ru1–Ru3** exhibited better *in vitro* antiproliferative activity than the ligand, **UA** and corresponding ruthenium polypyridyl chloride intermediate **A–C**, respectively. These indicated that introducing UA-piperazine-dithiocarbamate into ruthenium polypyridyl intermediate could improve the antitumor activity. Notably, **Ru1** and **Ru2** exhibited better antiproliferative activity than cisplatin on all the selected cancer cell lines, and the IC_{50} values were in the range of 0.73 ± 0.12 to 3.25 ± 0.50 μM. It is also important to note that **Ru3** displayed better inhibitory activity than cisplatin against T24, MDA-MB-231, and MCF-7 cells with IC_{50} values of 2.65 ± 0.37, 5.46 ± 0.32 and 14.63 ± 0.12 μM, respectively.

By comparing the *in vitro* antiproliferative activity of three complexes **Ru1–Ru3**, it was found that the nature of the ancillary ligands plays an important role in the antitumor activity of these complexes. When the complex incorporated two ancillary 1,10-phenanthroline ligands (**Ru2**), it had the lowest IC_{50} values in the MGC-803, T24, HepG2, and MDA-MB-231 cell lines. In the CNE2 and MCF-7 cell lines, the influence of the ancillary ligand on the antitumor activity of the complexes could be listed as follows: 2,2'-bipyridine > 1,10-phenanthroline > 4,7-diphenyl-1,10-phenanthroline. Our results may provide an example of tuning the selectivity of ruthenium complexes to different cancer cells by modifying the structure of the ancillary ligands.

To evaluate the resistance of complexes **Ru1–Ru3** to cisplatin, the MTT assay was carried out on A549 and its cisplatin-resistant cell line A549/DDP (Table S1). Three complexes exhibited significant antitumor activity toward A549 and A549/DDP, and it is noteworthy that complexes **Ru1–Ru3** displayed significant inhibition to A549/DDP with IC_{50} values of 2.66 ± 0.27, 3.95 ± 0.33, and 2.97 ± 0.14 μM, respectively, which were about 10-fold more potent than cisplatin (30.52 ± 0.17 μM). These results indicate that complexes could overcome the cisplatin resistance probably with a different anticancer mechanism.

Based on the significant antiproliferative activity on selected cell lines, **Ru1** and **Ru2** were chosen to further study the antiproliferative activity against MGC-803 multicellular spheroids. As shown in Fig. S4, treatment with **Ru1** and **Ru2** dramatically decreased the density of MGC-803 cancer cells, indicating the promising antitumor activity.

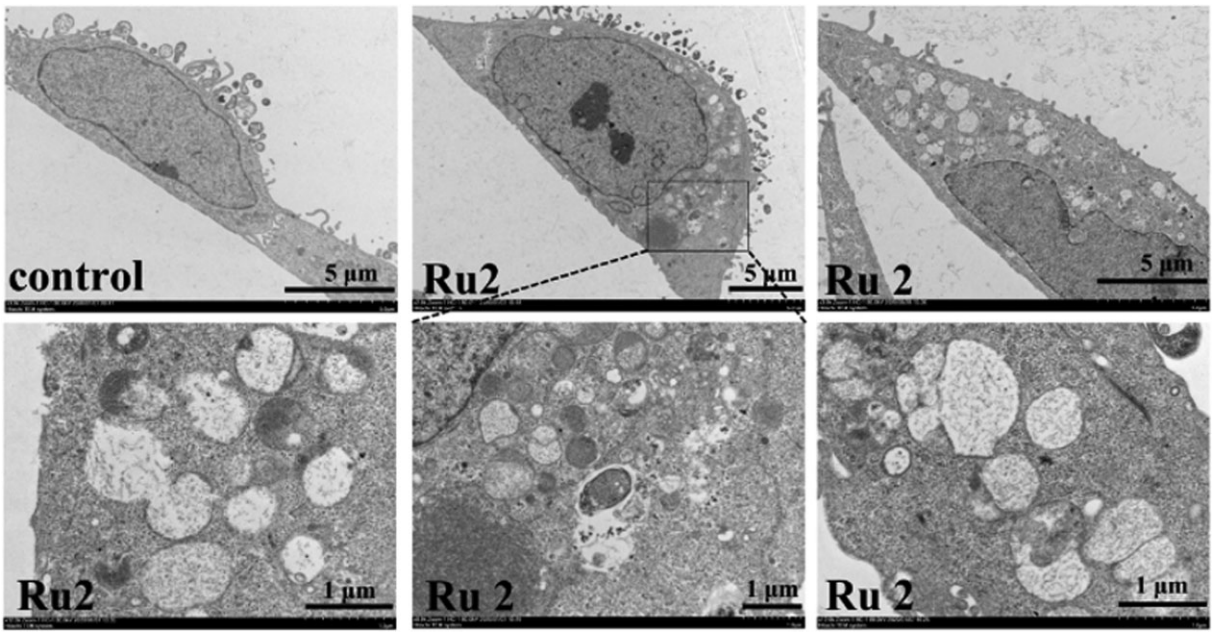

Fig. 3 Electron microscopy images of MGC-803cells treated with DMSO (control) or 2 μM **Ru2** for 24 h.

In vivo antiproliferative activity

The antitumoral activity of **Ru2** was then assessed for 27 days at two doses (6 mg/kg and 12 mg/kg) by tail vein injection once every 3 days. Specific pathogen-free BALB/c nude mice (both male and female) were divided randomly into four groups (n = 4), i.e. the vehicle control group, the low-dose and high-dose administration of **Ru2** groups, and the positive control groups. The dose of cisplatin was limited at 2 mg/kg owing to its severe toxicity.

As illustrated in Fig. 1A–D, the average tumor volume was 318 mm^3 for the control group and 207 mm^3 and 105 mm^3 for the low-dose and high-dose administration of **Ru2**, which were 34% and 67% lower than the control group. **Ru2** with an inhibition ratio of 64.8% ($P < 0.001$) at high doses exhibited higher suppression of tumor growth than cisplatin (47.3%, $P < 0.001$). This was despite it displaying comparable *in vivo* toxicity with cisplatin, which was investigated by monitoring the weight loss of all the tested nude mice. These results indicated that **Ru2** might be a good candidate for an antitumor agent.

Action mechanism investigation

LogP value and cellular accumulation of complexes

The ability of the Ru(II) complexes to penetrate cell membranes is generally attributed to their lipophilicity. Here, the lipophilicity of the Ru(II) complexes was examined by determining the octanol/water partition coefficients ($logP_{o/w}$) using the shake-flask method. The results (Table S2) indicated that **Ru1** exhibited the best hydrophilicity with a negative $logP_{o/w}$ value of –0.98 109, **Ru2** displayed moderate lipophilicity with a $logP_{o/w}$ of 0.428 897 and **Ru3** showed the highest lipophilicity with a $logP_{o/w}$ of 1.49 152. It is noted that increasing the aromatic surface area of the polypyridyl ligands resulted in increased lipophilicity of the complexes, and the order of logPo/w for these three complexes was **Ru1** < **Ru2** < **Ru3.**

The intracellular ruthenium concentrations in whole cells and cellular fractions of the complexes **Ru1**–**Ru3** were then investigated by inductively coupled plasma mass spectrometry (ICP-MS). As shown in Fig. 2A, the order for the dose of the three ruthenium complexes in whole cells was listed as follows: **Ru1** > **Ru2** > **Ru3**, which did not correlate and was even completely contrary to the trends observed in the $logP_{o/w}$ assay. It has been reported that the cellular uptake efficiencies of six classical coordinated (N-N) ruthenium polypyridyl complexes are positively correlated with their lipophilicities.[28] Here, we discover the inconsistency between lipophilicity and cellular uptake, which may be explained by introducing the UA-piperazine-dithiocarbamate ligand.

Combined with the MTT results, we could conclude that the sharply elevated cellular levels of ruthenium complexes might be one of the important reasons for the remarkable antiproliferative activity of **Ru1** and **Ru2**. Further investigation (Fig. 2B) indicated that the order for the proportion of ruthenium **Ru1** and **Ru2** in cellular fractions was membrane > cytoplasm > nuclear > cytoskeleton, implying that these two complexes mainly entered and stayed in the cell membrane.

ICP-MS for the uptake mechanism of Ru2 in MGC-803 cells

Ru2 exhibited the best antiproliferative effect among the three complexes and was selected as the representative compound for investigating possible cellular entry pathways. The aforementioned results implied that the order of the complexes accumulating in the cell was astonishingly inconsistent with the order of their lipophilicity. As mentioned in Poynton's 2017 review, the lipophilicity of complexes plays a very important role in passive diffusion, which is the main mechanism of uptake for metal complexes.[29] Thus, this inconsistency may illustrate that ruthenium complexes synthesized here may enter cells by facilitated diffusion, active transport, or endocytosis rather than passive diffusion.

Supporting this hypothesis, MGC-803 cells were treated with various conditions and inhibitors: 37°C (control group), 4°C (free diffusion group), D-deoxy-glucose and oligomycin (metabolic inhibited group), chloroquine (endosome acidity (endocytosis) inhibition group), and NH_4Cl (endosome-lysosome

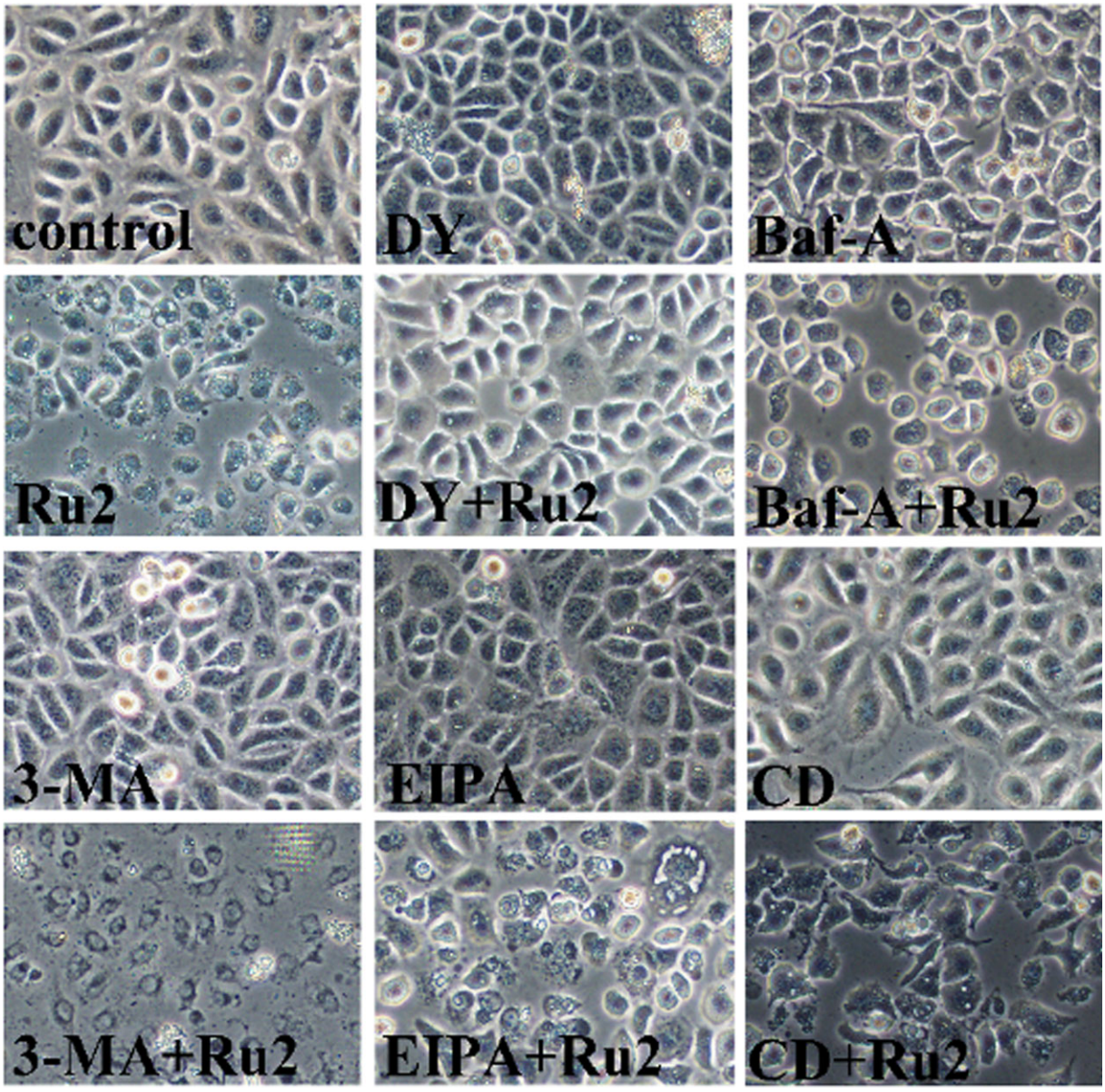

Fig. 4 MGC-803 cells were incubated with five inhibitors and were pretreated for 30 min in the presence or absence of specific inhibitors prior to addition of 2 μM **Ru2**. Phase-contrast images were taken after 24 h.

fusion (endocytosis) inhibition group). The cells were treated with **Ru2** for 1 h at 4°C or 2 h at 37°C. For the several well-documented inhibitor groups, the cells were incubated for 30 min with the corresponding inhibitor before treatment with 10 μM **Ru2** for 2 h. As shown in Fig. S5, compared with the control group, significantly decreased Ru levels were found at 4°C in the D-deoxy-glucose (oligomycin), chloroquine, and NH_4Cl groups, confirming the role of energy-dependent transport and the possibility of endocytosis, since these processes are responsible for the uptake of certain types of metal complexes.[30,31] To further determine the possible pathways of endocytosis, the specific inhibitors of chlorpromazine (clathrin-mediated endocytosis inhibition group) and nystatin (caveolae-mediated endocytosis inhibition group) were also employed to treat MGC-803 cells. The results displayed that chlorpromazine exhibited a significant inhibitory effect on the cellular uptake of **Ru2** instead of nystatin. This confirmed that clathrin-mediated endocytosis was the main mechanism by which **Ru2** entered the cells.

Transmission electron microscopy for cell morphology

The transmission electron microscope assay was performed on MGC-803 cells to investigate changes in cell morphology. Remarkably, treating MGC-803 cells with **Ru2** led to an accumulation of cytoplasmic vacuoles, as shown in Fig. 3. It is an interesting experimental phenomenon for ruthenium polypyridyl complex to induce tumor cell death. In 2017, Sun and co-workers discovered an UA-derived small molecule that could cause the accumulation of vacuoles derived from macropinosomes.[32] We wonder whether the mechanism of vacuolation induced by **Ru2** was associated with the compound reported in Sun's research and due to the presence of the UA-piperazine-dithiocarbamate ligand.

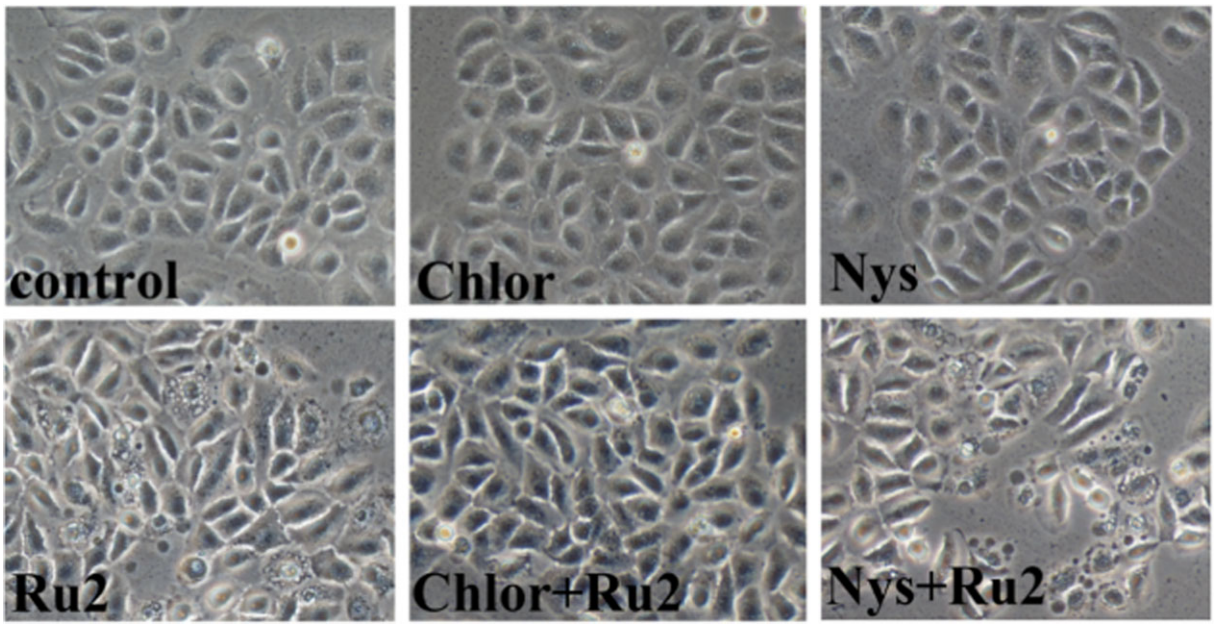

Fig. 5 MGC-803 cells were incubated with chlorpromazine or nystatin alone and were pretreated for 30 min in the presence or absence of two inhibitors prior to addition of 2 μM **Ru2**. Phase-contrast images were taken after 12 h.

Intracellular vesicle inhibition investigation

In considering the possible origins of the vacuole formation in MGC-803 cells, pharmacological treatments were carried out with inhibitors: bafilomycin A1 (Baf-A), a specific inhibitor of the vacuolar-type H^+-ATPase, which could block clathrin-independent endocytosis, like micropinocytosis; 5- (N-ethyl-N-isopropyl) amiloride (EIPA), an inhibitor of the Na^+/H^+ exchanger that blocks macropinocytosis and phagocytosis; 3-methyladenine (3-MA), which blocks the formation of autophagosomes by inhibiting class III PI3K.[33] The dynamin inhibitor dynasore (DY) and actin inhibitor cytochalasin D (CD) were also selected for investigating the pathways involved in the formation of intracellular vesicles after treatment with **Ru2**.

As shown in Fig. 4, in comparison with the treatment of **Ru2** alone, pre-incubation of MGC-803 cells with DY led to the disappearance of intracellular vesicles along with inhibition of cell death, which was consistent with the cell growth inhibition rate results (Fig. S6). When CD, 3-MA, and Baf-A were added before **Ru2** treatment, there was an obvious diminution of vacuoles, but cell viability was not blocked. Preincubation cells with EIPA neither blocked the formation of vesicles nor inhibited cell viability. These results demonstrated that the cytoplasmic vacuoles induced by **Ru2** were dynamin dependent, which was the critical regulator of clathrin-mediated endocytosis.[34] Furthermore, we could conclude that the vacuolization induced by **Ru2** was different from that induced by UA derivatives reported by Sun,[32] and the inhibition of **Ru2** internalization by DY resulted in the suppression of cytoplasmic vacuolation.

Clathrin-mediated endocytosis and siCHC2 RNA

Clathrin-mediated endocytosis or caveolin-mediated endocytosis is the main form of endocytosis. Our ICP-MS assay (Fig. S5) exhibited that **Ru2** entered the cells mainly by clathrin-mediated endocytosis. Prompted by the data showing that chlorpromazine could decrease the level of Ru, we asked whether the formation of cytoplasmic vacuoles could be blocked by chlorpromazine and whether downregulating clathrin heavy chain (CHC) expression with siRNA could modulate clathrin function. To support this hypothesis, chlorpromazine pretreatment and knocking down CHC with specific siRNAs were used in the **Ru2**-induced vacuolization assay.

As shown in Fig. 5, compared to the treatment with **Ru2** alone, pretreatment with chlorpromazine reduced the vacuoles in MGC-803 cells after a further 24-h incubation, while nystatin did not decrease the vacuoles. To further confirm the regulatory role of clathrin, disordered and longitudinal clathrin siRNAs were employed to treat MGC-803 cells in the presence and absence of **Ru2**. The results (Fig. 6) suggested that treatment with **Ru2** (1.5 and 2 μM) and disordered clathrin siRNA with **Ru2** (NC-Ru2) induced vacuolization in the MGC-803 cells. In contrast, siCHC treatment alone or co-incubation with siCHC and **Ru2** lessened the vacuoles in MGC-803 cells, implying that clathrin-mediated endocytosis was required for **Ru2** internalization and played an important role in cytoplasmic vacuolation.

Assay for lysosomal membrane permeabilization

It is known that lysosomes are the final destination of endocytosis. **Ru2** was found to be internalized into cells via clathrin-mediated endocytosis and deservedly accumulated in lysosomes. It is worth noting that the content of ruthenium in lysosomes diminished with prolonged incubation of **Ru2** with MGC-803 cells (Fig. S7), which suggested that **Ru2** could undergo lysosome escape. This could be proven by the lysosome assay with acridine orange (AO) staining. AO emits red fluorescence in acidic lysosomes and green fluorescence in the cytosol and nucleus. As shown in Fig. 7, treatment with **Ru2** significantly decreased the mean red fluorescence in the cells compared with the control cells since the stacked AO (red fluorescence) accumulated in the lysosomes. The result indicated that the lysosome integrity was damaged after treatment with **Ru2**, with consequent leakage of the AO into the cytosol and nucleus to stain the DNA or RNA (green fluorescence). In addition, the results confirmed that **Ru2** could escape from lysosome digestion.

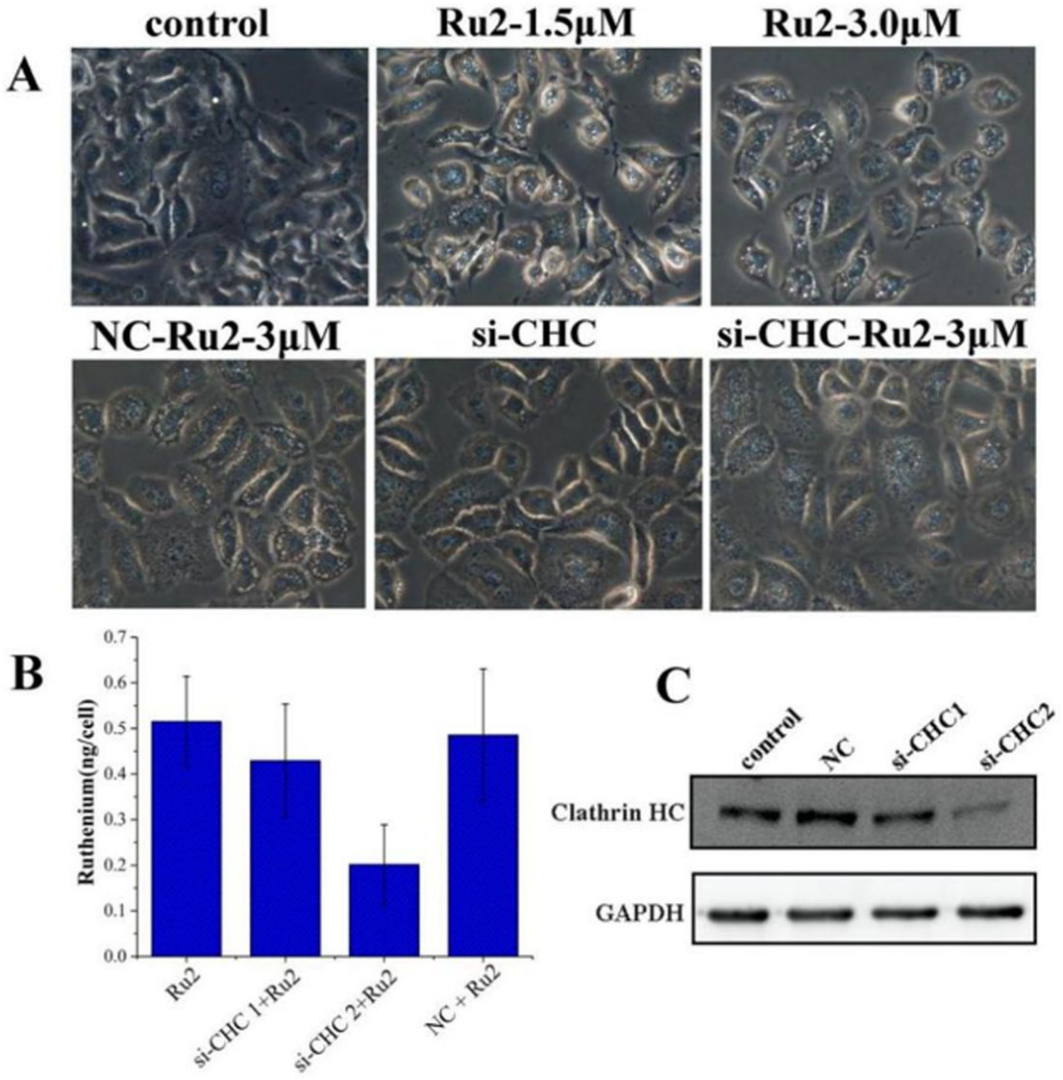

Fig. 6 Cytoplasmic vacuoles originated from mitochondria. (A) Cells were stained with 150 nM Mito-Tracker probe for 15 min after treatment with 2.0 μM **Ru2** for 12 h. Fluorescent and phase-contrast images were obtained by laser confocal microscopy. Scale bar, 50 μm. (B) Transmission electron microscopy images of microstructural changes in the mitochondria of MGC-803 cells incubated with 0, 0.5 and 2 μM **Ru2** for 24 h.

Dilation of mitochondria is the inducement of cytoplasmic vacuolation

Mitochondria play central roles in energy production and various metabolic activities. Therefore, it is an ideal target for therapeutic agents. One key characteristic of this organelle is the extremely negative membrane potential caused by the proton gradient across the mitochondrial inner membrane.[35] Considering this high negative potential of the outer membrane, we hypothesized that **Ru2** initially localized in the lysosomes by energy-dependent endocytosis and subsequently escaped and localized in the mitochondria due to its intrinsic cationic lipophilicity.

As mentioned in Fig. S6 and Fig. 4, treating MGC-803 cells with **Ru2** and dynasore/chlorpromazine could simultaneously suppress cytoplasmic vacuoles and cell death suggesting that the formation of vacuoles was pivotal for **Ru2**-induced cytotoxicity. To explore cytoplasmic vacuolation, mitochondria were labeled with Mito-Tracker Red (MTR) (Fig. 8A). Integrated, compact, reticulate shapes were observed around the nucleus in the control group. In contrast, dilated and swollen mitochondria appeared in the **Ru2**-treated cells. However, there was no similar observation with the endoplasmic reticulum-tracker under the same experimental condition (Fig. S8). Dilated mitochondria were further confirmed by transmission electron microscopy (Fig. 8B), which clearly showed the formation of cytoplasmic vacuoles after treatment with **Ru2** at 0.5 and 2.0 μM for 24 h. The vacuoles are the double-membrane organelles. Together, these observations demonstrated that vacuoles were the result of dilated and swollen mitochondria induced by **Ru2**.

Cell death mode investigation

The mode of cell death induced by antitumor agents is of great significance for investigating their mechanism of action. To determine the mode of cell death induced by **Ru2**, necrostatin-1 (a necroptosis inhibitor), leupeptin (a lysosome pathway-associated cell death inhibitor), Z-VAD-FMK (an apoptosis inhibitor), cycloheximide (a paraptosis inhibitor), and 3-methyladenine (an autophagy inhibitor) were employed with **Ru2** to treat MGC-803 cells. As shown in Fig. S9, the cell growth inhibition rate at 1.5 μM **Ru2** was significantly reduced in the presence of necrostatin-1 and leupeptin, indicating that death of the MGC-803 cells was by necroptosis and related to lysosomes.

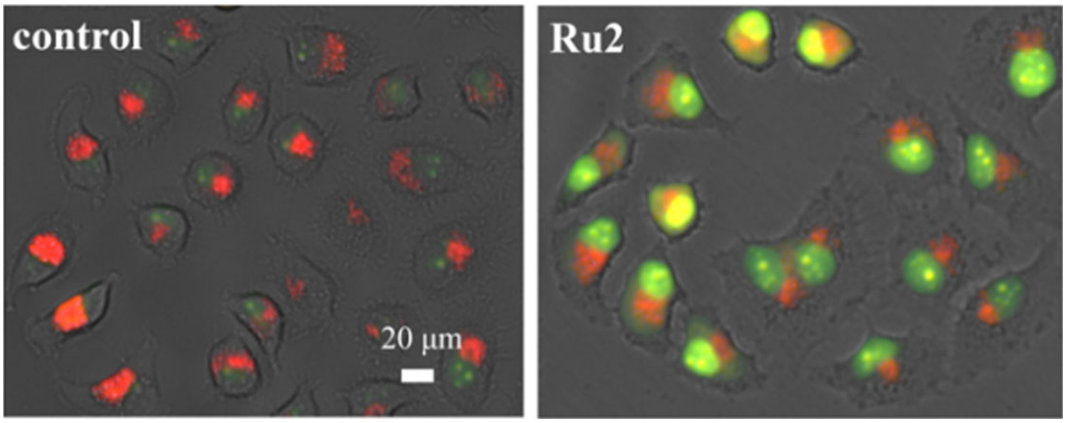

Fig. 7 Fluorescence images of MGC-803 cells loaded with acridine orange.

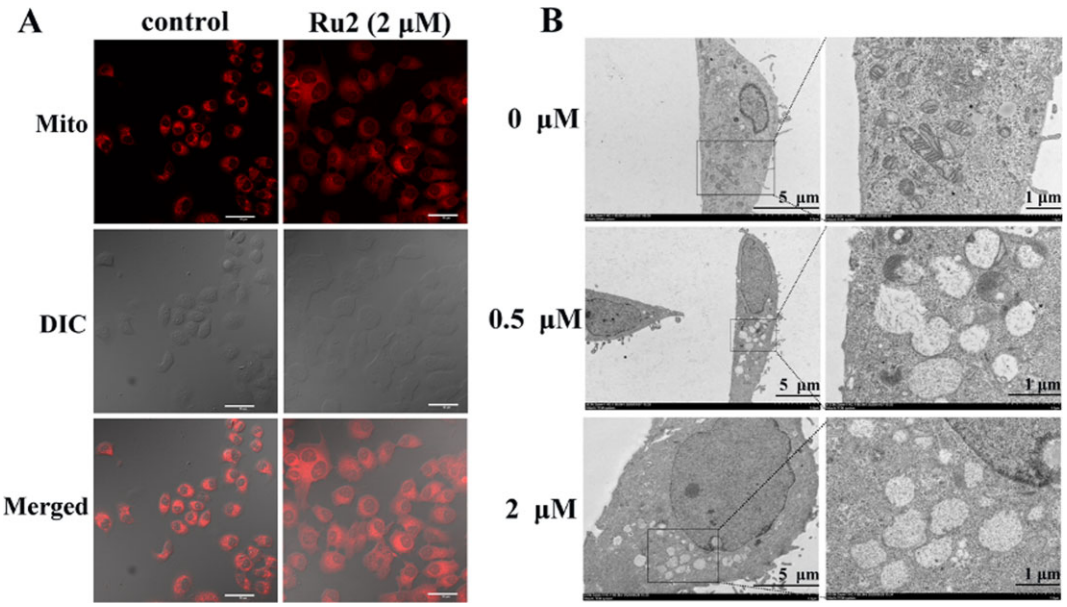

Fig. 8 Cytoplasmic vacuoles originated from mitochondria. (A) Cells were stained with 150 nM Mito-Tracker probe for 15 min after treatment with 2.0 μM **Ru2** for 12 h. Fluorescent and phase-contrast images were obtained by laser confocal microscopy. Scale bar, 50 μm. (B) Transmission electron microscopy images of microstructural changes in the mitochondria of MGC-803 cells incubated with 0, 0.5 and 2 μM **Ru2** for 24 h.

Intracellular ROS

Mitochondria are the main source of ROS production. **Ru2** could induce dilation of mitochondria. Moreover, mitochondrial ROS are known to be involved in necroptosis.[36] With these facts in mind, the commercial ROS fluorescent probe 6-carboxy-2′,7′-dichlorodihydrofluorescein diacetate (DCFH-DA) was employed to evaluate the intracellular generation of ROS. As shown in Fig. S10, MGC-803 cells treated with **Ru2** (2 μM for 12 h) exhibited stronger green fluorescence than the untreated control cells (in black), confirming the intracellular ROS overproduction.

Hoechst 33258/propidium iodide double staining assay

Cells encountering necroptosis usually exhibit classical necrosis-like morphological characteristics, including cell swelling and membrane rupture.[37–39] To further investigate whether treatment with **Ru2** could induce necroptosis, the Hoechst 33258/propidium iodide (PI) double staining assay was performed with MGC-803 cells. The blue fluorescent Hoechst dyes are cell-permeable nucleic acid stains, while PI is membrane impermeant and generally excluded from viable cells. In view of the different characteristics of these two dyes, PI is used for identifying dead cells probably undergoing necroptosis. As shown in Fig. 9, the results indicated that treatment with **Ru2** led to a decrease in the blue fluorescence in Hoechst 33258 staining and an increase in the red fluorescence in PI staining implying the occurrence of necroptosis.

RIP1–RIP3 complex

Necroptosis is the best-characterized programmed necrosis and modulated in a receptor-interacting protein kinase 1 (RIPK1)- and 3 (RIPK3)-dependent manner. RIPK1, RIPK3, and their substrate, mixed-lineage kinase domain-like protein (MLKL), function as pivotal proteins in executing necroptosis and compose a necrosome complex.[8–10] And the formation of functional necrosomes can be promoted by ROS production.[40] As mentioned above, necrostatin-1, a potent RIP1 kinase inhibitor, attenuated the cell growth inhibition rate at 1.5 μM **Ru2** treatment in the mode of cell death

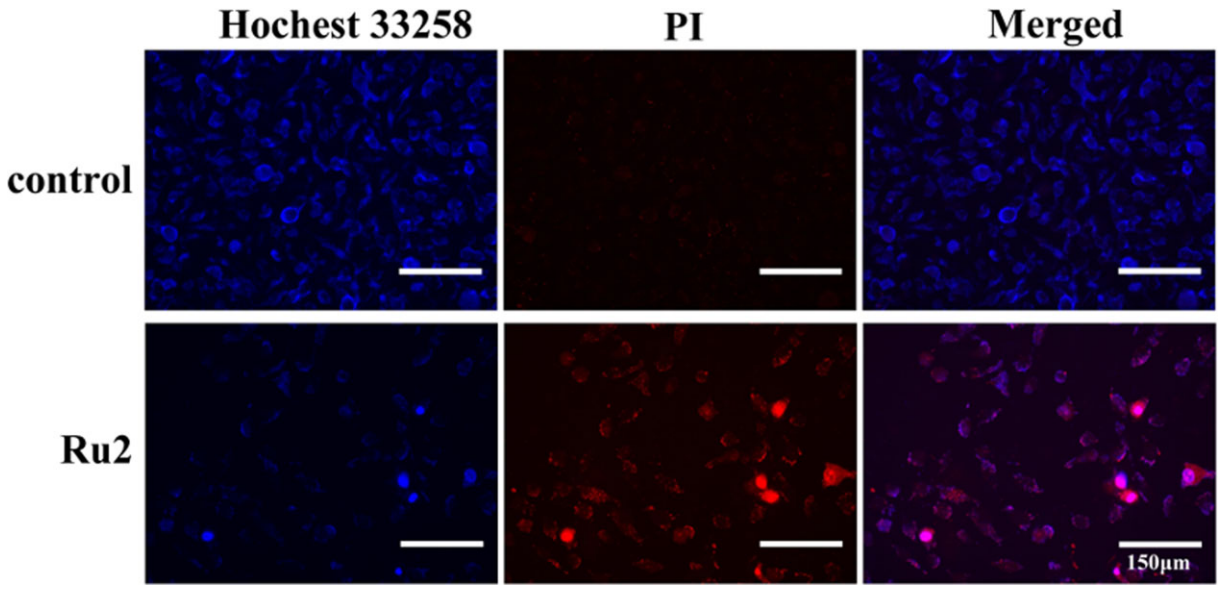

Fig. 9 Fluorescence microscopy images of MGC-803 cells untreated and treated with **Ru2** (2 μM for 24 h), then stained with Hoechst 33258 and PI.

experiments. Therefore, immunoblotting was carried out to study the expression of RIP1, RIP3, and MLKL, as well as their phosphorylated proteins. The results (Fig. S11) indicated that treatment with **Ru2** in a series of concentrations (0, 0.5, 1, and 2 μM) for 24 h could upregulate the expressions of p-RIP1 Ser 166, p-RIP3, and p-MLKL. These findings suggested that RIP1, RIP3, and MLKL were involved in the **Ru2**-induced necroptosis. In addition, the upregulation of p- RIP3 at ser227 was confirmed by an immunofluorescence assay (Fig. S12) in which the green fluorescence indicated the expression of p-RIP3 and the blue fluorescence located the nuclei. Compared with the control, treatment with **Ru2** (2 μM, 24 h) enhanced the green fluorescence. Together, our data showed that the formation of necrosomes containing RIP1 and RIP3 was a key regulator in **Ru2**-induced necroptosis.

Conclusion

In this study, we designed and synthesized three UA-piperazine-dithiocarbamate ruthenium(II) complexes **Ru1** – **Ru3** to screen as antitumor agents. MTT screening results showed that **Ru1** and **Ru2** exhibited better antiproliferative effects than the clinically used cisplatin on all the selected cancer cell lines, including MGC-803, T24, HepG2, CNE2, MDA-MB-231, A549, and MCF-7 with IC_{50} values in the range of 0.73 ± 0.12 to 3.25 ± 0.50 μM. **Ru3** displayed better inhibition than cisplatin against T24, MDA-MB-231, and MCF-7 with IC_{50} values of 2.65 ± 0.37, 5.46 ± 0.32, and 14.63 ± 0.12 μM, respectively. MGC-803 multicellular spheroids and xenograft mouse models assays exhibited that **Ru2** should be a promising effective antitumor. By the comparison of the antitumor activities of **Ru1–Ru3** with dehydroabietyl piperazine dithiocarbamate ruthenium(II) polypyridyl complexes in our previous work, respectively,[24] it should be concluded that the replacement of **UA** skeleton of dehydroabietyl group could lead to better antitumor activity. In addition, **Ru1–Ru3** could overcome the cisplatin resistance by exhibiting antiproliferative activity on A549/DDP. We found that representative **Ru2** initially localized in the lysosomes by energy-dependent endocytosis and subsequently escaped and accumulated in the mitochondria. This localization resulted in the swelling and dilation of mitochondria, which was the origin of cytoplasmic vacuolation. Cell death pathway inhibition assays showed that **Ru2**-induced MGC-803 cell death was necroptosis and related to lysosomes. Furthermore, upregulation of the expression levels of p-RIP1(Ser 166), p-RIP3(Ser 227), and p-MLKL (Ser 358) was observed in western blot assays, indicating that **Ru2**-induced necroptosis was primarily modulated by the activation of RIP1 and RIP3, which phosphorylated MLKL. In conclusion, **Ru2** could act as a chemotherapeutic agent to kill cancer cells via vacuolation-associated cell death and RIP1-dependent necroptosis. These dual mechanisms could be key factors for the high activity and overcoming cisplatin resistance of **Ru2**.

Experimental

Materials and instruments

All chemicals in the synthetic experiments and the materials used for the biological assays were commercially available and used without further purification. The NMR spectra, HR-MS, HPLC, and EA were measured on a BRUKER ESQUIRE HCT spectrometer, BRUKER ESQUIRE HCT spectrometer, shimazuLC-20A HPLC instrument and PE2400II element analyzer, respectively.

Synthetic procedure of ligand (L) and its complexes Ru1–Ru3

A mixture of **UAP** (10 mmol) and sodium hydroxide aqueous solution (10 mmol NaOH in 1 ml water) was stirred in 50 ml ethanol, and excess carbon disulfide (100 mmol) was added dropwise and reacted for 2 h. After the reaction, a white powder ligand (**L**) was obtained through vacuum evaporation and purified by silica column chromatography using dichloromethane–methanol (v: v = 250:3) solution as the eluent. The mixture of **L** (1 mmol), dipyridine ruthenium intermediate (1 mmol), tetramethyl ammonium hydroxide aqueous solution (1 ml), and dichloromethane-methanol solution (20 ml, volume ratio 2:1) was stirred and reacted at 65°C for 24 h. After the reaction, the red powder complexes **Ru1–Ru3** were obtained through vacuum evaporation and then purified by neutral alumina column chromatography using dichloromethane–methanol (v: v = 100:2) solution as the eluent. The characterization data were listed as below.

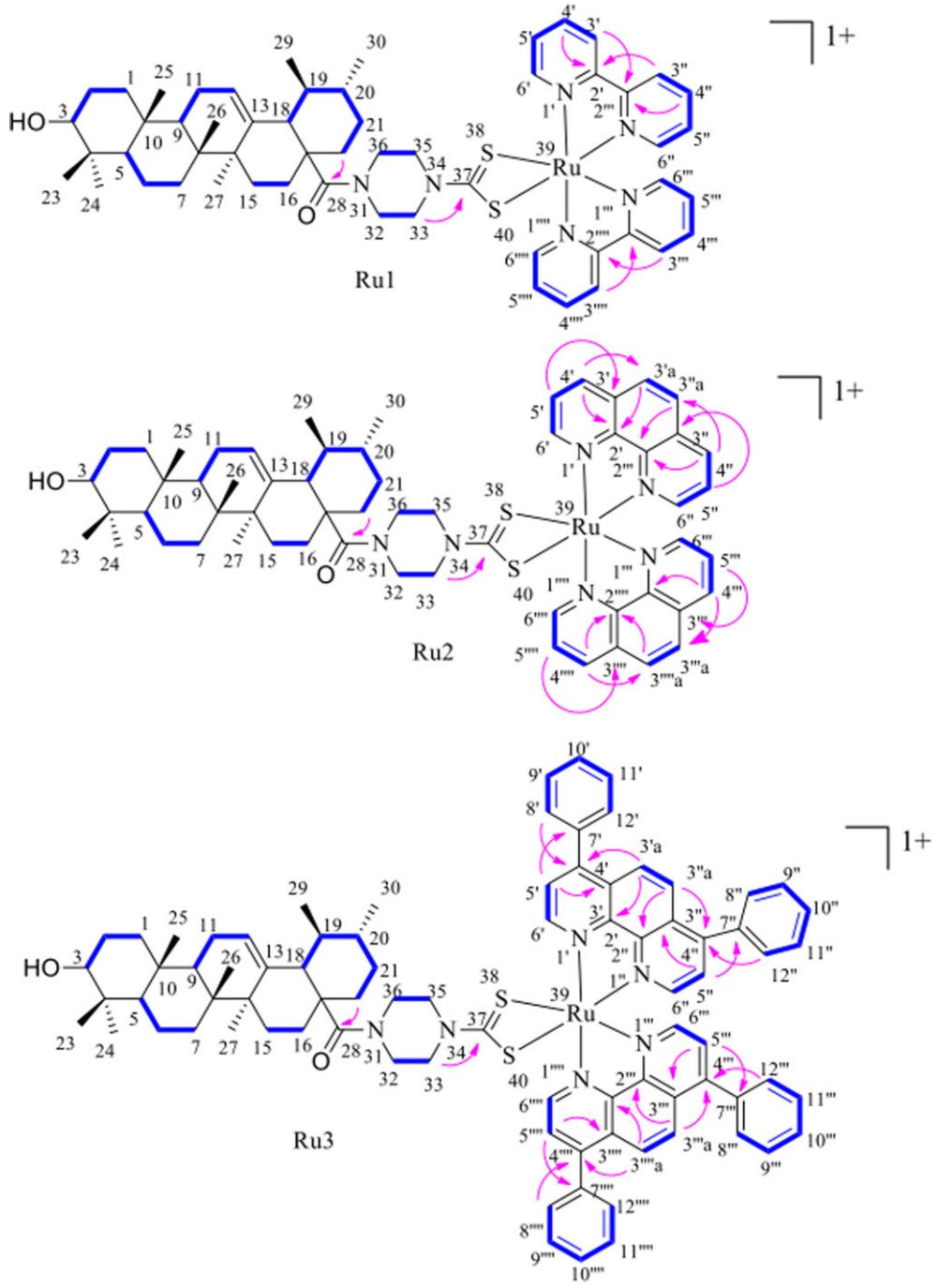

Fig. 10 Key HMBC (arrows) and ^{1}H-^{1}H COSY (bonds) correlations of **Ru1**–**Ru3**.

Ligand **L**: Yields 72.8%. ^{1}H NMR (500 MHz, DMSO-d_6) δ 5.30 (s, 1H, OH), 5.09 (s, 1H, 12-H), 4.35–3.51 (br, 9H, 3-H and 4 × CH_2 in piperazine), 3.04–2.94 (br, 1H), 2.35 (d, J = 10.5 Hz, 1H), 2.00 (dd, J = 69.7, 59.1 Hz, 6H), 1.57–1.13 (m, 14H), 1.03 (s, 3H, 27-CH_3), 0.92 (d, J = 5.1 Hz, 4H, 26-CH_3 and CH), 0.88 (s, 3H, 25-CH_3), 0.86–0.81 (m, 6H, 23-CH_3 and 24-CH_3), 0.66 (s, 3H, 29-CH_3), 0.65 (s, 3H, 30-CH_3) ppm. ^{13}C NMR (126 MHz, DMSO-d_6) δ 194.45(C = S), 174.97(C = O), 139.00 (C = C), 124.85 (C = C), 77.30, 55.33, 51.40, 51.34, 49.50, 48.28, 47.57, 44.65, 44.64, 38.83, 38.70, 37.00, 33.95, 32.94, 30.49, 29.59, 29.35, 28.72, 27.47, 25.85, 23.37, 21.53, 18.45, 17.75, 16.80, 16.52, 15.69 ppm. HRMS (m/z) (ESI): $C_{35}H_{55}N_2NaO_2S_2$[**L** + Na]$^+$ calcd for: 645.3500, found: 645.3601; $C_{35}H_{55}N_2NaO_2S_2$[**L**-Na]$^-$ calcd for: 599.3705, found: 599.3714.

Complex **Ru1**: Yields 63.4%. ^{1}H NMR (500 MHz, DMSO-d_6) δ: 8.77 (d, J = 7.9 Hz, 2H, H-3′,3‴), 8.15 (t, J = 7.5 Hz, 2H, H- H-4′,4‴), 7.86 (t, J = 7.6 Hz, 2H, H-5′,5‴), 9.51 (d, J = 4.9 Hz, 2H, H-6′,6‴), 8.67 (d, J = 7.9 Hz, 2H, H-3″, 3‴), 7.91 (t, J = 7.6 Hz, 2H, H-4″,4‴), 7.31 (t, J = 7.6 Hz, 2H, H-5″,5‴), 7.66 (d, J = 4.8 Hz, 2H, H-6″,6‴), 3.00 (br s, 1H, H-3), 4.34 (s, 1H, 3-OH), 1.82 (m, 4H, H-7a,11b,15a, 22b), 2.05 (m, 1H, H-11a), 5.06 (s, 1H, H-12), 2.32 (d, J = 10.4 Hz, 1H, H-18), 2.02 (s, 1H, H-22a), 1.20-1.44 (m, 19H), 0.89 (s, 6H, H-23,30), 0.66 (s, 3H, H-24), 0.64 (s, 3H, H-25), 0.83 (s, 6H, H-26,29), 1.02 (s, 3H, H-27), 3.84

(br s, 4H, H-32,36), 3.58 (br s, 4H, H-33,35) ppm; ^{13}C NMR (125 MHz, DMSO-d_6) δ: 36.5 (C-1), 27.0 (C-2), 76.8 (C-3), 38.2 (C-4), 54.8 (C-5), 17.9 (C-6), 32.7 (C-7), 39.9 (C-8), 47.0 (C-9), 38.2 (C-10), 22.8 (C-11), 124.4 (C-12), 138.2 (C-13), 40.1 (C-14), 27.6 (C-15), 29.0 (C-16), 39.9 (C-17), 54.8 (C-18), 38.4 (C-19), 38.4 (C-20), 30.0 (C-21), 33.4 (C-22), 28.2 (C-23), 16.1 (C-24), 15.2 (C-25), 16.4 (C-26), 23.6 (C-27), 174.6 (C-28), 17.3 (C-29), 21.0 (C-30), 47.0 (C-32,36), 46.2 (C-33,35), 212.0 (C-37), 157.5 (C-2′,2‴), 123.6 (C-3′,3‴), 135.2 (C-4′,4‴), 127.0 (C-5′,5‴), 153.5 (C-6′,6‴), 157.8 (C-2″,2‴), 123.4 (C-3″,3‴), 135.9 (C-4″,4‴), 126.4 (C-5″,5‴), 151.0 (C-6″,6‴) ppm. The key HMBC and ^{1}H-^{1}H COSY correlations of **Ru1** was shown in Fig. 10. Anal. Calcd. for [$C_{55}H_{71}N_6O_2RuS_2$]Cl: C, 62.98; H, 6.82; N, 8.01. Found: C, 62.91; H, 6.74; N, 8.10. HRMS (m/z) (ESI): ($C_{55}H_{71}N_6O_2RuS_2^+$) $[M]^+$ calcd for: 1013.4123, found: 1013.4136.

Complex **Ru2**: Yields 64.1%. ^{1}H NMR (500 MHz, DMSO-d_6) δ: 8.81 (d, J = 8.2 Hz, 2H, H-4′,4‴), 8.26 (m, 2H, H-5′,5‴), 9.87 (d, J = 5.1 Hz, 2H, H-6′,6‴), 8.49 (d, J = 8.1 Hz, 2H, H-4″,4‴), 7.52 (dd, J = 8.1, 5.3 Hz, 2H, H-5″,5‴), 7.92 (d, J = 5.3 Hz, 2H, H-6″,6‴), 8.37 (d, J = 8.9 Hz, 2H, H-3'a,3‴a), 8.22 (m, 2H, H-3″a,3‴a), 3.00 (m, 1H, H-3), 4.34 (s, 1H, 3-OH), 1.82 (m, 4H, H-7a,11b,15a, 22b), 2.04 (m, 2H, H-11a,22a), 5.06 (s, 1H, H-12), 2.32 (d, J = 11.1 Hz, 1H, H-18), 1.20-1.44 (m, 19H), 0.89 (s, 6H, H-23,30), 0.66 (s, 3H, H-24), 0.63 (s, 3H, H-25), 0.81 (s, 6H, H-26,29), 1.02 (s, 3H, H-27), 3.85 (br s, 4H, H-32,36), 3.59 (br s, 4H, H-33,35) ppm; ^{13}C NMR (125 MHz, DMSO-d6) δ: 36.5 (C-1), 27.0 (C-2), 76.8 (C-3), 38.2 (C-4), 54.8 (C-5), 18.0 (C-6), 32.7 (C-7), 40.0 (C-8), 48.0 (C-9), 38.2 (C-10), 22.9 (C-11), 124.4 (C-12), 138.6 (C-13), 40.1 (C-14), 27.6 (C-15), 29.0 (C-16), 40.0 (C-17), 54.8 (C-18), 38.4 (C-19), 38.4 (C-20), 30.0 (C-21), 33.4 (C-22), 28.3 (C-23), 16.1 (C-24), 15.2 (C-25), 16.4 (C-26), 24.0 (C-27), 174.6 (C-28), 17.3 (C-29), 21.0 (C-30), 47.0 (C-32,36), 46.2 (C-33,35), 212.2 (C-37), 148.5 (C-2′,2‴), 129.8 (C-3′,3‴), 134.3 (C-4′,4‴), 126.0 (C-5′,5‴), 154.9 (C-6′,6‴), 148.1 (C-2″,2‴), 130.1 (C-3″,3‴), 134.8 (C-4″,4‴), 125.1 (C-5″,5‴), 152.0 (C-6″,6‴), 127.9 (C-3'a,3‴a), 127.4 (C-3″a,3‴a) ppm. The key HMBC and ^{1}H-^{1}H COSY correlations of **Ru2** was shown in Fig. 10. Anal. Calcd. for [$C_{59}H_{71}N_6O_2RuS_2$]Cl: C, 64.60; H, 6.52; N, 7.66. Found: C, 64.53; H, 6.59; N, 7.74. HRMS (m/z) (ESI): ($C_{59}H_{71}N_6O_2RuS_2^+$)[M]$^+$ calcd for: 1061.4123, found:1061.4137.

Complex **Ru3**: Yields 64.1%. ^{1}H NMR (500 MHz, DMSO-d_6) δ: 8.26 (m, 2H, H-5′,5‴), 10.01 (d, J = 5.3 Hz, 2H, H-6′,6‴), 7.82 (m, 4H, H-8′,8‴,12′,12‴), 7.56 (m, 4H, H-9′,9‴,11',11‴), 7.65 (m, 4H, H-10′,10″,10‴,10‴), 8.22 (m, 2H, H-5″,5‴), 8.25 (m, 2H, H-6″,6‴), 8.24 (m, 2H, H-3'a,3‴a), 8.12 (m, 2H, H-3″a,3‴a), 2.96 (m, 1H, H-3), 4.34 (s, 1H, 3-OH), 1.77 (m, 4H, H-7a,11b,15a, 22b), 2.04 (m, 2H, H-11a,22a), 5.03 (s, 1H, H-12), 2.31 (d, J = 10.9 Hz, 1H, H-18), 1.20-1.44 (m, 19H), 0.85 (d, J = 7.2 Hz, 6H, H-23,30), 0.62 (m, 6H, H-24,25), 0.77 (m, 6H, H-26,29), 0.99 (s, 3H, H-27), 3.78 (m, 8H, H-32,33,35,36) ppm; ^{13}C NMR (125 MHz, DMSO-d_6) δ: 36.5 (C-1), 27.0 (C-2), 76.8 (C-3), 38.1 (C-4), 54.8 (C-5), 17.9 (C-6), 32.6 (C-7), 39.9 (C-8), 48.0 (C-9), 38.1 (C-10), 22.8 (C-11), 124.3 (C-12), 136.0 (C-13), 39.9 (C-14), 27.7 (C-15), 29.0 (C-16), 39.8 (C-17), 54.8 (C-18), 38.3 (C-19), 38.3 (C-20), 30.0 (C-21), 33.4 (C-22), 28.2 (C-23), 16.0 (C-24), 15.2 (C-25), 16.4 (C-26), 22.1 (C-27), 174.6 (C-28), 17.2 (C-29), 21.0 (C-30), 47.0 (C-32,36), 46.3 (C-33,35), 211.9 (C-37), 149.2 (C-2′,2‴), 127.7 (C-3′,3‴), 145.4 (C-4′,4‴), 125.4 (C-5′,5‴), 154.5 (C-6′,6‴), 135.7 (C-7′,7‴), 130.0 (C-8′,8‴,12',12‴), 129.2 (C-9′,9‴,11′,11‴), 129.7 (C-10′,10‴), 148.9 (C-2″,2‴), 127.5 (C-3″,3‴), 146.1 (C-4″,4‴), 125.9 (C-5″,5‴), 152.1 (C-6″,6‴), 136.0 (C-7″,7‴), 129.2 (C-8″,8‴,12″,12‴), 129.0 (C-9″,9‴,11″,11‴), 129.7 (C-10″,10‴), 126.2 (C-3'a,3‴a), 125.9 (C-3″a,3‴a) ppm. The key HMBC and ^{1}H-^{1}H COSY correlations of **Ru3** was shown in Fig. 10. Anal. Calcd. for [$C_{83}H_{87}N_6O_2RuS_2$]Cl: C, 71.14; H, 6.26; N, 6.00. Found: C, 71.06; H, 6.34; N, 6.09. HRMS (m/z) (ESI): ($C_{83}H_{87}N_6O_2RuS_2$)[M]$^+$ calcd for: 1365.5375, found: 1365.5505.

Biological assays

The materials, procedures, and instruments for the biological assays, including cell culture and transfections, electron microscopy, metal distribution, cellular uptake, lysosomal membrane permeabilization (acridine orange assay), intracellular ROS, immunofluorescence analysis, and western blot assays are depicted in the Supplementary Data (Part 1, †ESI).

Supplementary material

Supplementary data are available at *Metallomics* online.

Funding

This study was supported by the Guangxi Natural Science Foundation (Nos. 2020GXNSFFA325001, 2020GXNSFAA297167 and 2016GXNSFAA380300), National Natural Science Foundation of China (Nos. Nos. 82160657, 82104008 and 32060108), Guangxi New Century Ten, Hundred and Thousand Talents Project ([2017]42), Guangxi Science and Technology Base and Talents Program (AD20297059), Guangxi Key Laboratory of Agricultural Resources Chemistry and Biotechnology (2019KF02), and State Key Laboratory for Chemistry and Molecular Engineering of Medicinal Resources (CMEMR2020-B05).

Data availability

The data underlying this article will be shared on reasonable request to the corresponding author.

Conflicts of interest

There are no conflicts to declare.

References

1. G. Szakacs, J. K. Paterson, J. A. Ludwig, C. Booth-Genthe and M. M. Gottesman, Targeting multidrug resistance in cancer, *Nat. Rev. Drug Discovery*, 2006, 5 (3), 219–234.
2. P. Bouwman and J. Jonkers, The effects of deregulated DNA damage signalling on cancer chemotherapy response and resistance, *Nat. Rev. Cancer*, 2012, 12 (9), 587–598.
3. S. W. Lowe, E. Cepero and G. Evan, Intrinsic tumour suppression. *Nature*, 2004, 432 (7015), 307–315.
4. K. M. Debatin and P. H. Krammer, Death receptors in chemotherapy and cancer, *Oncogene*, 2004, 23 (16), 2950–2966.
5. L. H. Hurley, DNA and its associated processes as targets for cancer therapy, *Nat. Rev. Cancer*, 2002, 2 (3), 188–200.
6. W. Zhou and J. Y. Yuan, Necroptosis in health and diseases, *Semin. Cell Dev. Biol.*, 2014, 35, 14–23. doi: 10.1016/j.semcdb.2014.07.013.
7. S. J. Lanhouet, F. Riquet, L. Duprez, T. V. Berghe, N. Takahashi and P. Vandenabeele, Necroptosis, in vivo detection in experimental disease models, *Semin. Cell Dev. Biol.*, 2014, 35, 2–13. doi: 10.1016/j.semcdb.2014.08.010.
8. J. X. Li, T. M. Quade, A. B. Siemer, J. Napetschnig, K. Moriwaki, Y. S. Hsiao, E. Damko, D. Moquin, T. Walz, A. McDermott, F. K. Chan and H. Wu, The RIP1/RIP3 necrosome forms a functional amyloid signaling complex required for programmed necrosis, *Cell*, 2012, 150 (2), 339–350.
9. K. M. Irrinki, K. Mallilankaraman, R. J. Thapa, H. C. Chandramoorthy, F. J. Smith, N. R. Jog, R. K. Gandhirajan, S. G. Kelsen, S. R.

Houser, M. J. May, S. Balachandran and M. Madesh, *Mol. Cell. Biol.*, 2011, 31 (18), 3745–3758.
10. C. J. Huang, Y. N. Luo, J. W. Zhao, F. W. Yang, H. W. Zhao, W. H. Fan and P. F. Ge, Shikonin kills glioma cells through necroptosis mediated by rip-1. *PLoS One*, 2013, 8 (6), e66326.
11. O. A. Lenis-Rojas, C. Roma-Rodrigues, A. R. Fernandes, F. Marques, D. Perez-Fernandez, J. Guerra-Varela, L. Sanchez, D. Vazquez-García, M. Lopez-Torres, A. Fernandez and J. J. Fernandez, Dinuclear RuII(bipy)2 derivatives: structural, biological, and in vivo zebrafiish toxicity evaluation, *Inorg. Chem.*, 2017, 56 (12), 7127–7144.
12. M. R. Gill and J. A. Thomas, Ruthenium(II) polypyridyl complexes and DNA - from structural probes to cellular imaging and therapeutics. *Chem. Soc. Rev.*, 2012, 41 (8), 3179–3192.
13. Q. Q. Yu, Y. N. Liu, L. Xu, C. P. Zheng, F. L. Le, X. Y. Qin, Y. Y. Liu and J. Liu, Ruthenium(II) polypyridyl complexes: Cellular uptake, cell image and apoptosis of HeLa cancer cells induced by double targets. *Eur. J. Med. Chem.*, 2014, 82, 82–95. doi: 10.1016/j.ejmech.2014.05.040.
14. K. Xiong, C. Qian, Y. X. Yuan, L. Wei, X. X. Liao, L. T. He, W. R. Thomas, Y. Chen, J. Wan, L. N. Ji and H. Chao, Necroptosis induced by ruthenium(II) complexes as dual catalytic inhibitors of topoisomerase I/II, *Angew. Chem. Int. Ed.*, 2020, 59 (38), 16631–16637.
15. H. Xu, X. Zhao, X. Liu, P. Xu, K. Zhang and X. Lin, Antitumor effects of traditional Chinese medicine targeting the cellular apoptotic pathway. *Drug Des. Dev. Ther.*, 2015, 9, 2735–2744. doi: 10.2147/DDDT.S80902.
16. L. Yang, X. Z. Liu, Z. B. Lu, J. Y. W. Chan, L. L. Zhou, K. P. Fung, P. Wu and S. H. Wu, Ursolic acid induces doxorubicin-resistant HepG2 cell death via the release of apoptosis-inducing factor. *Cancer Lett.*, 2010, 298 (1), 128–138.
17. J. S. Wang, L. Q. Liu, H. J. Qiu, X. H. Zhang, W. Guo, W. B. Chen, Y. Tian, L. Y. Fu, D. B. Shi, J. D. Cheng, W. L. Huang and W. G. Deng, Ursolic acid simultaneously targets multiple signaling pathways to suppress proliferation and induce apoptosis in colon cancer cells. *PLoS One*, 2013, 8 (5), e63872.
18. S. Prasad, V. R. Yadav, B. Sung, S. Reuter, R. Kannappan, A. Deorukhkar, P. Diagaradjane, C. M. Wei, V. Baladandayuthapani, S. Krishnan, S. Guha and B. B. Aggarwal, Ursolic acid inhibits growth and metastasis of human colorectal cancer in an orthotopic nude mouse model by targeting multiple cell signaling pathways: chemosensitization with capecitabine. *Clin. Cancer Res.*, 2012, 18 (18), 4942–4953.
19. S. X. Hua, R. Z. Huang, M. Y. Ye, Y. M. Pan, G. Y. Yao, Y. Zhang and H. S. Wang, Design, synthesis and in vitro evaluation of novel ursolic acid derivatives as potential anticancer agents, *Eur. J. Med. Chem.*, 2015, 95, 435–452. doi: 10.1016/j.ejmech.2015.03.051.
20. C. C. Lu, B. R. Huang, P. J. Liao and G. C. Yen, Ursolic acid triggers nonprogrammed death (necrosis) in human glioblastoma multiforme DBTRG-05MG cells through MPT pore opening and ATP decline, *Mol. Nutr. Food Res.*, 2014, 58 (11), 2146–56.
21. J. P. Luzio, P. R. Pryor and N. A. Bright, Lysosomes: fusion and function, *Nat. Rev. Mol. Cell Biol.*, 2007, 8 (8), 622–632.
22. Z. Skrott, M. Mistrik, K. K. Andersen, S. Friis, D. Majera, J. Gursky, T. Ozdian, J. Bartkova, Z. Turi, P. Moudry, M. Kraus, M. Michalova, J. Vaclavkova, P. Dzubak, I. Vrobel, P. Pouckova, J. Sedlacek, A. Miklovicova, A. Kutt, J. Li, J. Mattova, C. Driessen, Q. P. Dou, J. Olsen, M. Hajduch, B. Cvek, R. J. Deshaies and J. Bartek, Alcohol-abuse drug disulfiram targets cancer via p97 segregase adaptor NPL4, *Nature*, 2017, 552 (7684), 194–199.
23. E. M. Nagy, L. Ronconi, C. Nardon and D. Fregona, Noble metal-dithiocarbamates precious allies in the fight against cancer, *Mini Rev. Med. Chem.*, 2012, 12 (12), 1216–1229.
24. H. Wang, J. Wei, H. Jiang, Y. Zhang, C. Jiang and X. Ma, Design, synthesis and pharmacological evaluation of three novel dehydroabietyl piperazine dithiocarbamate ruthenium(II) polypyridyl complexes as potential antitumor agents: DNA aamage, cell cycle arrest and apoptosis induction, *Molecules*, 2021, 26 (5), 1453.
25. Y. L. Li, X. M. Zhu, N. F. Chen, S. T. Chen, H. Liang and Z. F. Chen, Anticancer activity of ruthenium(II)plumbagin complexes with polypyridyl as ancillary ligands via inhibiting energy metabolism and GADD45A-mediated cell cycle arrest. *Eur. J. Med. Chem.*, 2022, 236, 114312. doi: 10.1016/j.ejmech.2022.114312.
26. G. B. Jiang, W. Y. Zhang, M. He, Y. Y Gu, L. Bai, Y. J. Wang, Q. Y. Yi and F. Du, Systematic evaluation of the antitumor activity of three ruthenium polypyridyl complexes. *J. Inorg. Biochem.*, 2021, 225, 111616. doi: 10.1016/j.jinorgbio.2021.111616.
27. Y. S. Liu, Q. Q. Li, M. J. Gu, D. S. Lu, X. X. Xiong, Z. Y. Zhang, Y. N. Pan, Y. Q. Liao, Q. H. Ding, W. X. Gong, D. S. Chen, M. T. Guan, J. Z. Wu, Z. Q. Tian, H. Deng, L. J. Gu, X. C. Hong and Y. L. Xiao, A second near-infrared Ru(II) polypyridyl complex for synergistic chemo-photothermal therapy. *J. Med. Chem.*, 2022, 65 (3), 2225–2237.
28. M. R. Gill and J. A. Thomas, Ruthenium(II) polypyridyl complexes and DNA—from structural probes to cellular imaging and therapeutics, *Chem. Soc. Rev.*, 2012, 41 (8), 3179–3192.
29. F. E. Poynton, S. A. Bright, S. Blasco, D. C. Williams, J. M. Kelly and T. Gunnlaugsson, The development of ruthenium(II) polypyridyl complexes and conjugates for in vitro cellular and in vivo applications, *Chem. Soc. Rev.*, 2017, 46 (24), 7706–7756. doi: 10.1039/C7CS00680B.
30. I. Romero-Canelón, A. M. Pizarro, A. Habtemariam and P. J. Sadler. Contrasting cellular uptake pathways for chlorido and iodido iminopyridine ruthenium arene anticancer complexes, *Metallomics*, 2012, 4 (12), 1271–1279.
31. C. A. Puckett, R. J. Ernst and J. K. Barton, Exploring the cellular accumulation of metal complexes, *Dalton Trans.*, 2010, 39 (5), 1159–1170.
32. L. Sun, B. Li, X. H. Su, G. Chen, Y. Q. Li, L. Q. Yu, L. Li and W. G. Wei, an ursolic acid derived small molecule triggers cancer cell death through hyperstimulation of micropinocytosis. *J. Med. Chem.*, 2017, 60 (15), 6638–6648.
33. E. F. Blommaart, U. Krause, J. P. Schellens, H. VreelingSindelarova and A. J. Meijer, The phosphatidylino- sitol 3-kinase inhibitors wortmannin and LY294002 inhibit autophagy in isolated rat hepatocytes, *Eur. J. Biochem.*, 1997, 243 (1-2), 240–246.
34. J. E. Hinshaw, Dynamin and Its Role in Membrane Fission, *Annu. Rev. Cell Dev. Biol.*, 2000, 16 (1), 483–519.
35. R. R. Ye, J. J. Cao, C. P. Tan, L. N. Ji and Z. W. Mao, Valproic acid-functionalized cyclometalated Iridium (III) complexes as mitochondria-targeting anticancer agents, *Chem. Eur. J.*, 2017, 23 (60), 15166–15176.
36. Z. T. Yang, Y. Wang, Y. Y. Zhang, X. D He, C. Q Zhong, H. X. Ni, X. Chen, Y. J Liang, J. F Wu, S. M. Zhao, D. W. Zhou and J. H. Han, RIP3 targets pyruvate dehydrogenase complex to increase aerobic respiration in TNF-induced necroptosis, *Nat. Cell Biol.*, 2018, 20 (2), 186–197.
37. A. Kaczmarek, P. Vandenabeele and D. V Krysko, Necroptosis: the release of damage-associated molecular patterns and its physiological relevance, *Immunity*, 2013, 38 (2), 209–223.

38. J. Sosna, S. Voigt, S. Mathieu, A. Lange, L. Thon, P. Davarnia, T. Herdegen, A. Linkermann, A. Rittger, F. Ka-Ming Chan, D. Kabelitz, S. Schütze and D. Adam, TNF-induced necroptosis and PARP-1-mediated necrosis represent distinct routes to programmed necrotic cell death Cell. *Cell. Mol. Life Sci.*, 2014, 71 (2), 331–348.
39. X. S. Xu, C. C. Chua, M. Zhang, D. Q. Geng, C. F. Liu, R. C. Hamdy and Balvin H. L. Chua, The role of PARP activation in glutamate-induced necroptosis in HT-22 cells, *Brain Res.*, 2010, 1343, 206–212.
40. Y. Y. Zhang, S. S. Su, S. B. Zhao, Z. T. Yang, C. Q. Zhong, X. Chen, Q. X. Cai, Z. H. Yang, D. L. Huang, R. Wu and J. H. Han, RIP1 autophosphorylation is promoted by mitochondrial ROS and is essential for RIP3 recruitment into necrosome, *Nat. Commun.*, 2017, 8 (1), 14329.